

We are IntechOpen, the world's leading publisher of Open Access books Built by scientists, for scientists

6,500

Open access books available

177,000

International authors and editors

195M

Downloads

Our authors are among the

154

Countries delivered to

TOP 1%

most cited scientists

12.2%

Contributors from top 500 universities



WEB OF SCIENCE™

Selection of our books indexed in the Book Citation Index
in Web of Science™ Core Collection (BKCI)

Interested in publishing with us?
Contact book.department@intechopen.com

Numbers displayed above are based on latest data collected.
For more information visit www.intechopen.com



Chapter

Analysis and Modeling of Polygonality in Retinal Tissue Based on Voronoi Diagram and Delaunay Tessellations

Nazario Bautista-Elivar and Ricardo Cruz-Castillo

Abstract

Several important properties of biological systems are directly related and even determined by the spatial distribution of their constituent elements. Those elements interact with each other and tend to use space in an optimal way, regarding their specific function and environmental constraints. A detailed methodology, based on Voronoi polygons and Delaunay triangles method employed to extract information on the spatial distribution of cells, is presented. On the other hand, diabetic retinopathy (DR) is defined as microvascular pathology. However, some data have suggested that the retinal photoreceptor (RPs) might be important in the pathogenesis of this ocular disease. In this study, the organization of the PRs in control and diabetic-induced rats was compared, using multiphoton microscopy. The PR mosaic was imaged at different locations in non-stained retinas. Thus, this work investigated the pathological changes in the cellular structures of the retina in the early stages of diabetes in laboratory animals. Of the different proposed tools that are highly reliable to be tested with human retinas, the metrics mean averaged distance and the mean square deviation of the angles are found ($P < 0.05$).

Keywords: multiphoton microscopy, diabetic retinopathy, Voronoi tessellations, computational geometry, bioinformatics

1. Introduction

Several biological/physical systems involve two-dimensional spatial arrangements with elements such as molecules, or cellular tissue, and the profiling in space has important repercussions to biological and physical investigations. The analysis of biological tissues often requires quantitative measurements to explore cell organization, in order to understand, identify, and monitor changes during pathology development and healing processes.

Measurements of cellular organization might not be always able to distinguish healthy and diseased tissues from each other [1]. It has also been revealed that the existing density measurements in cells present multiple restrictions [2–7]. In

particular, some studies have reported that the density of retinal cones is not an appropriate parameter to identify pathological states in early stages of retina diseases [8, 9].

Maps of cellular distribution have to be considered linked to morphogenesis, mechanical structural stabilities and functional state of a given healthy tissue. Finding the connection that links form to disorder and is based on distance networks partition constructed from the position of cells when defined as mathematical nodes generators of Voronoi tessellations, then they can be used to construct summary functions [10], see **Table 1**. For example, Sudbø and Marcelponil Reith developed 27 algorithms based on Voronoi diagrams to describe the architecture of tissues [11]. Chiu showed that the minimum angles and areas of Delaunay triangles are responsive parameters when it concerns cellular distributions [12]. Voronoi analysis has also been used to determine the packing arrangement of cones at different retinal storage bins displayed with adaptive optics (AO) and hexagonal packing was found [13, 14]. Other authors have proposed to measure the regularity of convex polygons by successive measurements of irregular polygonal reconfiguration until regularity [15].

However, side number, distance between cones, according to proportion, any measurements derivative from the least distance will cause statistics to fail to identify healthy tissues and pathological tissues, which yield identical statistical densities measured from the shortest distances [1]. Other serious constraints developed from the method of counting the number of Voronoi cell sides result

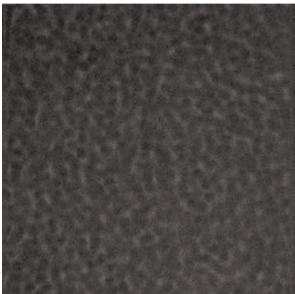
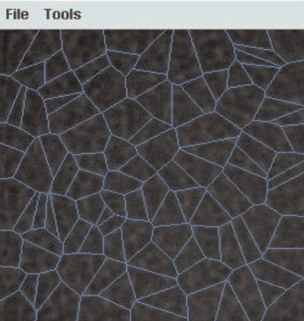
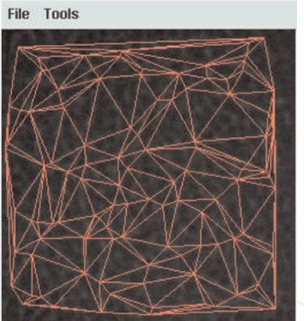
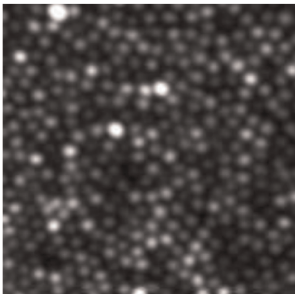
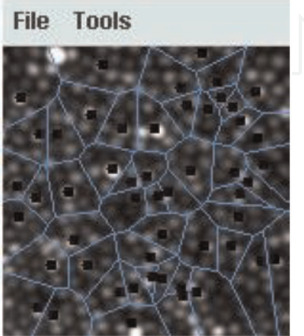
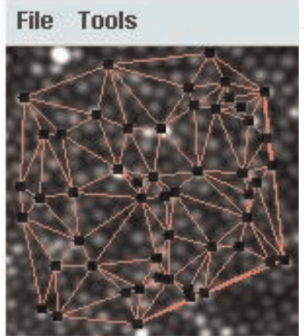
Retinal photoreceptor	Real image (healthy tissues)	Voronoi polygon	Delaunay triangulation
Sprague-Dawley male rat	 Multiphoton microscope	 File Tools	 File Tools
Human	 Adaptive optics scanning laser ophthalmoscope (AOSLO)	 File Tools	 File Tools

Table 1.
Voronoi polygons and Delaunay triangles in a retinal tissue.

from the fact that the number of cell sides will not change except for gross perturbations of the particle system. In addition, in Delaunay triangulation, no significant differences are observed by using Delaunay segments and Delaunay areas in tissues [16].

The general aim of this chapter is to establish an analysis for a comparison of the distribution of PRs in tissues with retinopathy diabetic, which is an important problem to mechanically understanding of the processes that lead to the experimental observations. This research presents only the model of the photoreceptor's spatial location (cones and sticks) considering photoreceptors small enough, in the suitable scale, to contemplate them as mathematical points. Then, Voronoi polygons and Delaunay triangles are formed by using these points. Therefore, Voronoi polygons do not represent the photoreceptor's shape. So, in this chapter, Voronoi polygons are not used to model biological cells nor their surrounding tissues.

This chapter is organized as follows: in Section 2, the description of several metrics using Voronoi polygon and Delaunay triangles and its integrated platform based on computational geometry, is given; in Section 3, multiphoton microscopy and image analysis is provided; in Section 4 we continue with a detailed description of retinal tissues, using Voronoi and Delaunay metrics described in Section 2; the Discussion is presented in Section 5, and finally the Conclusions are in Section 6.

2. Metrics/algorithm to computational biology

2.1 Description of metrics/algorithm

2.1.1 Internal distance

The internal distance d_i in a particular Voronoi cell, is the distance measured from the internal mathematical node (black dot, see **Figure 1**) of the Voronoi polygon to each neighboring point (blue dot, see **Figure 1**) which forms the polygon. This is an Ulam tree modified to measure distances, **Figure 1**.

2.1.2 Angular graph

The numbers ψ_i are the angles between the horizontal line which contains the internal mathematical node and the line which joins each neighboring point to the internal node, it is measured anticlockwise (Ulam tree modified to angles), **Figure 2**.

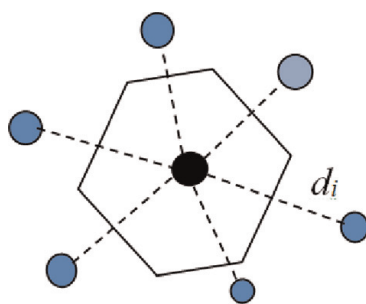


Figure 1.
Distance graph (Ulam tree modified) between neighbors in a 6-sided Voronoi polygon.

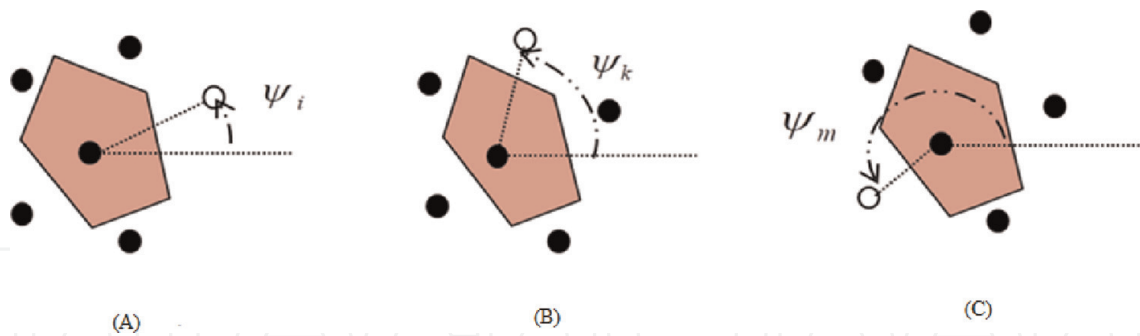


Figure 2.
Angle measurement between nearby points from a horizontal axis.

2.1.3 Internal angles of Delaunay triangles

These are the internal angles of any triangle in the Delaunay triangulation ω_i ; the angles are measured in the positive direction (counterclockwise), **Figure 3**, using the following procedure:

- i. First, measure the angle between two points containing the generating interior point of each cell.
- ii. Arrange angles from least to greatest.
- iii. Then measure the edge distances of the Delaunay triangulation containing the generating point.
- iv. Finally, measure the angle between consecutive edges in which such a vertex is the generating point.

The sequence to measure the angle ω_i is in the following order: if you select first point 1 (vertex 1) then select point 2 (vertex 2), these points will form a starting line where the angle measurement starts, the point 3 (vertex 3) is where the angle measured ends. The selection and sequence of generating points will indicate the final angle obtained.

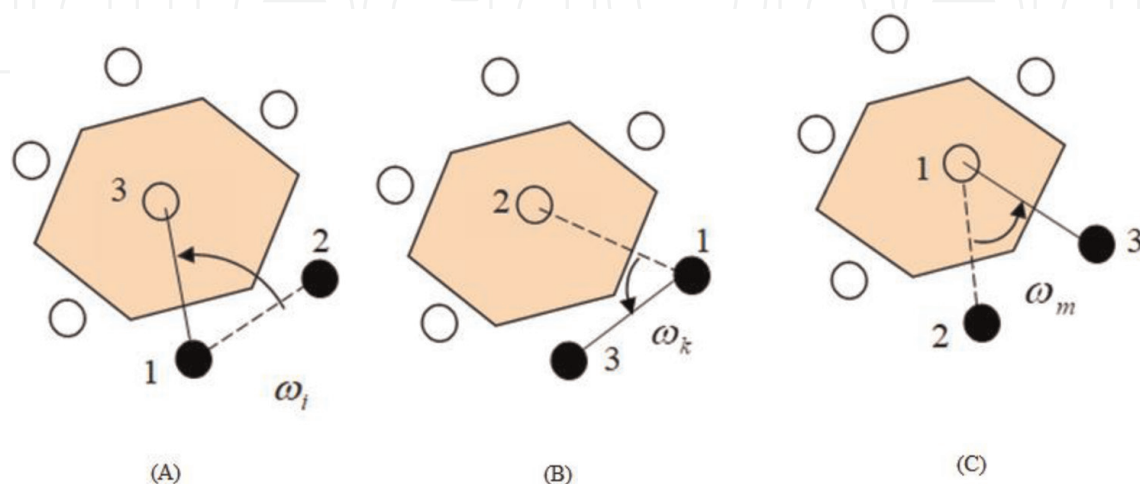


Figure 3.
Procedure to measure angles between three neighbors that form a Voronoi polygon and choosing one angle.

2.1.4 Mean distances average

This metric/algorithm determine the mean of average distances from the inner point in every Voronoi cell to its n neighbors and it is calculated by

$$\sum_{i=1}^n \frac{d_i}{n^2} \quad (1)$$

where d_i is the internal distance defined above. It also represents a way to measure the cell size and it could be interpreted as a coefficient of expansion or contraction, **Figure 4**.

2.1.5 Polygonality index

This metric/algorithm generates the measure Ξ ,

$$\Xi = \frac{1}{\sum_{i=1}^n |\chi_i - \beta| + 1} \quad (2)$$

where χ_i is the formed angle between consecutive neighbors for Delaunay triangle (irregular polygon, dotted arrow), β is the angle between consecutive vertex for a regular polygon (solid arrow), $\beta = 360 \text{ degree}/n$ and n is the number of neighbors of the Voronoi cell, **Figure 5**. The angle χ_i is invariant under any rotation movement. The measurement is performed counterclockwise.

If the value of Ξ is close to 1, then the Voronoi polygon is close to regularity, angles χ_i and β will have similar value. If Ξ is close to 0, then Voronoi polygon is irregular. The units of Ξ is the inverse in degrees.

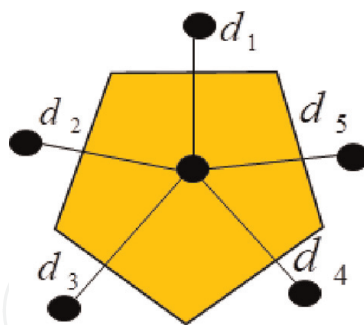


Figure 4.
 Modified Ulam tree graph to measure distances in Voronoi cell.

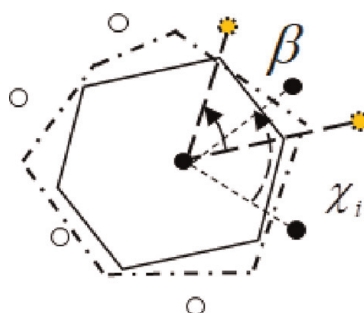


Figure 5.
 The solid line is a regular polygon, the irregular polygon is represented by the dotted line, and the neighbors are the black circle. The internal black dot is a mathematical node.

2.1.6 Mean-square deviation of angles

This metrics/algorithms evaluate ε ,

$$\varepsilon = \sqrt{\sum_{i=1}^n (\chi_i - \beta)^2} \quad (3)$$

the root square of mean deviation from the angles χ_i , with respect to angle $\beta = 360 \text{ degree}/n$ where n is the number of neighbors of the Voronoi cell for each Voronoi polygon. The magnitudes χ_i , β , and n are defined above (**Figure 5**). The metric ε is invariant under any rotation movement.

2.1.7 Variation index angle of differences

This metric algorithm gets δ ,

$$\delta = \frac{1}{\sqrt{\sum_{i=1}^n (\chi_i - \beta)^2 + 1}} \quad (4)$$

where χ_i and $\beta = 360 \text{ degree}/n$ are defined as above (**Figure 5**). If the value of δ is close to 1, then the Voronoi polygon is close to regularity, if δ is close to 0, then Voronoi polygon is irregular.

2.2 Software description

In view of the foregoing, we suggest development of an integrated platform based on computational geometry for bioinformatics and computational biology for analyzing spatial cellular organization which in turn use both Voronoi tessellation and Delaunay triangulation, for the purpose to measure the distance, internal angles, radius of circumscribed circle, amid nearby points mean distances average, angular polygonality, polygonality index, mean-square deviation of angles, and variation index angle of differences. The platform holds two options, either being performed by a user or operating with an automatic formulation. This software allows to create Voronoi polygons and Delaunay triangles from a set of XY coordinates, or generated by selecting in an imported image. It locates XY coordinates, using an auxiliary window S, **Figure 6**.

2.2.1 Voronoi frequency

This function displays graphics of frequency with respect to the number of sides in Voronoi mosaic with a data reading window, wider enough to avoid loss of data of polygons compared to other platforms [17].

2.2.2 Circumscribed circle

These metrics/algorithms are able to find the magnitude of the circumradius, the coordinates of the center of the circumcircle, and the coordinates of the vertices formed in each Delaunay triangle. R is the radius of the circle circumscribing a Delaunay triangle, some examples (a) and (b), **Figure 7**.

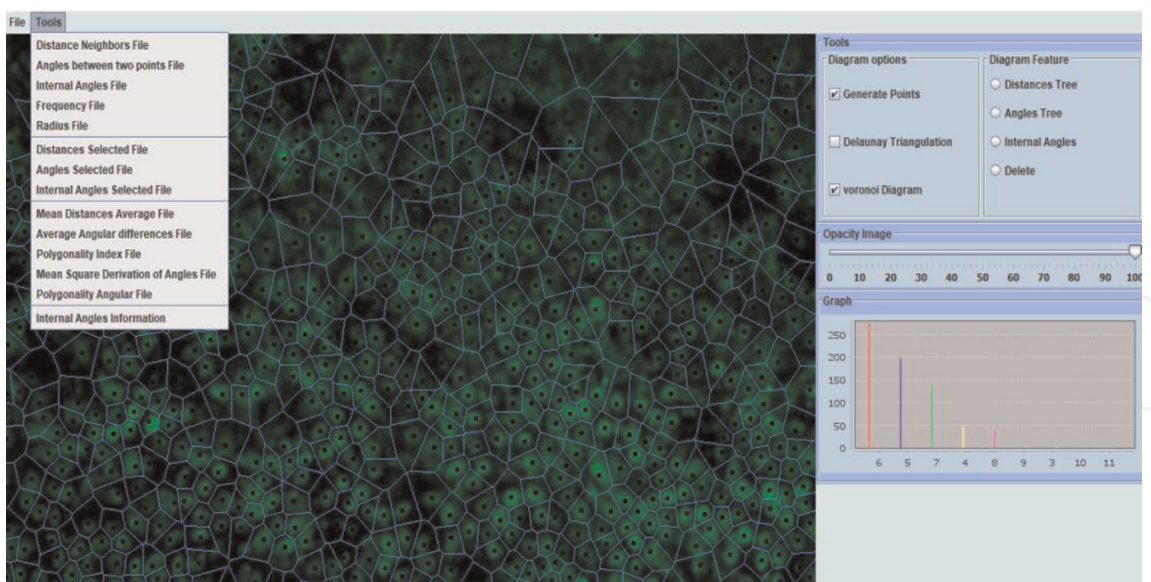


Figure 6.
 Platform based on computational geometry for Voronoi polygons and Delaunay triangles to biological structures.

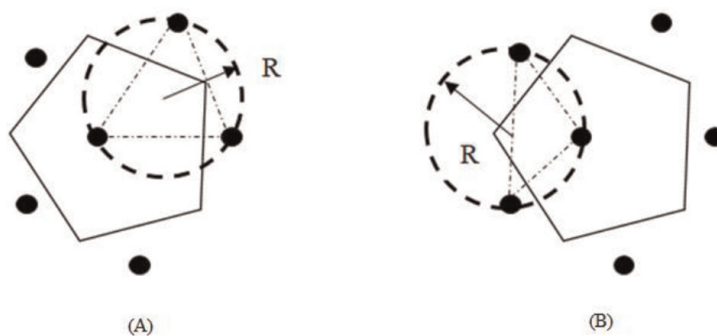


Figure 7.
 Circumcircle and circumradius for each Delaunay triangle in a Voronoi polygon.

2.2.3 Distances selected

These metrics/algorithms are able to get the distance d_k between each pair of points selected by the user. First select the icon distances, located in Diagram Feature screen, after that choose a point of the polygon, by the icon select points, then select again the icon select point for another interest point, finally activate the icon selected file distances from Tools menu to get the data file with its coordinates and the distance that separates them. You might select different pairs of points to find out their distances in a single file, activating the icon selected for several couple points, for example (A), (B), (C), **Figure 8**.

2.2.4 Angles selected

These metrics/algorithms generate a file formed from each pair of points selected by the user. The angle ν is relative to the horizontal axis and it works as the rangefinder. First, activate the *angles tree* icon (**Figure 6**), and then you can select different points for the same file using the select point button, to generate the Angles Selected file, **Figure 9**.

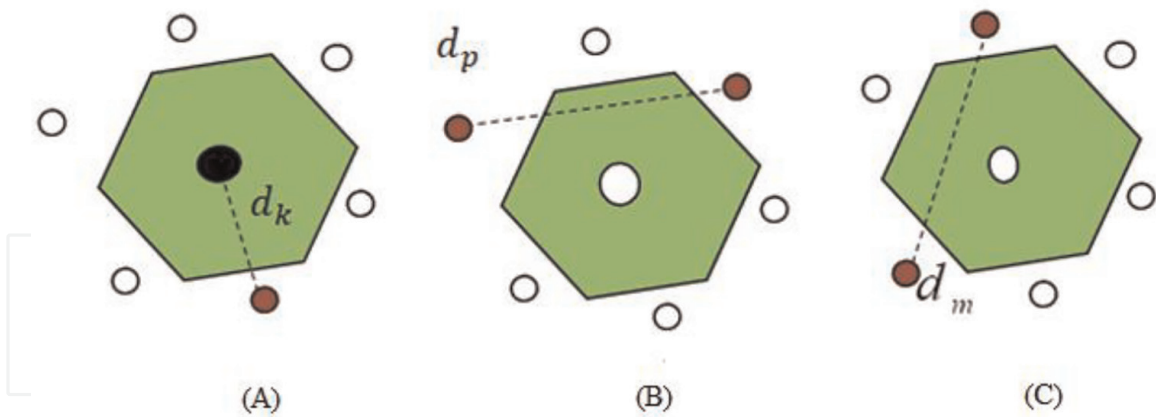


Figure 8.
Selection of distances to be chosen by the user in a Voronoi polygon.

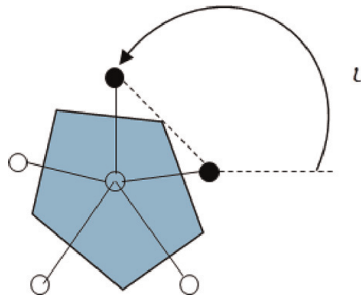


Figure 9.
Selection of angles between neighbors to be chosen by the user in a Voronoi polygon.

Internal angles selected. This metric algorithm generates a file for the angles γ_i of each Delaunay triangle selected by the user. First, activate radio button internal angles (Figure 6), then select points radio button to form the Delaunay triangle, selecting three points. The select order of each point defines the angle to be measured. First, if the black point is selected, then you can choose the white point. These two points form a line from which we start measuring the angle and ends at the line formed between the third point, the striped circle, forming an angle which is measured from for example, tree forms to obtain several internal angles in a Delaunay triangle, $\gamma_k, \gamma_p, \gamma_i$, Figure 10, (A), (B) and (C), respectively.

For example, for four tides polygon, if the option 2 is selected, the angle γ_i is shown in Figure 11.

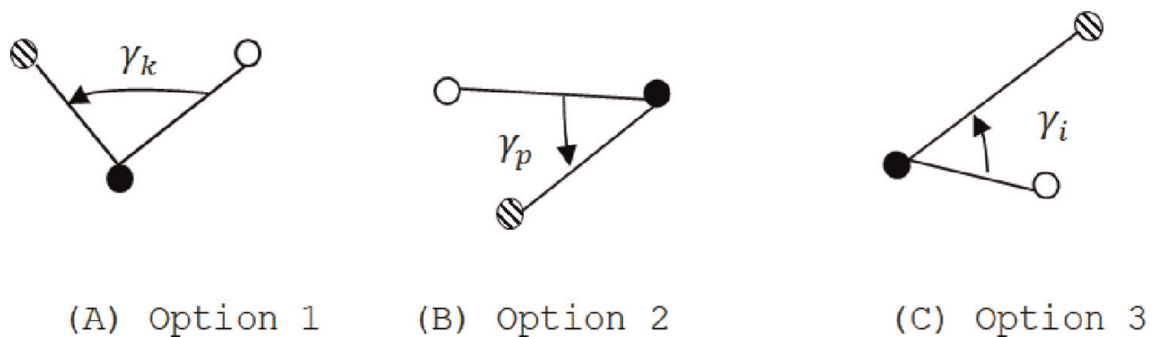


Figure 10.
Options to select nearby points to get an angle between them in a Voronoi mosaic.

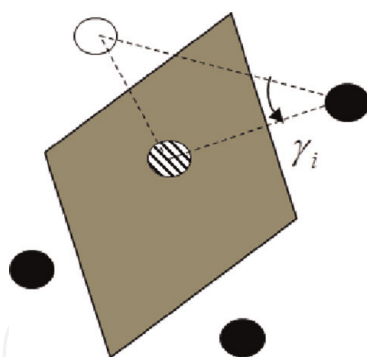


Figure 11.
 Delaunay triangle, an angle selected between neighbors with option 2, Figure 10.

3. Multiphoton microscopy, image acquisition and processing

A multiphoton microscope was used to obtain images of the retinal mosaic in 16 healthy (C) mice and sixteen mice with diabetic retinopathy (DR). The multiphoton microscope combines a fs-laser system (760 nm), a scanning unit, a Z-motor, and a detector (photon-counting) within an inverted microscope. The whole system was computer-controlled. Nonlinear microscopy images were acquired using two imaging modalities: regular XY images and fast 2-photon imaging tomography, **Figure 12**.

Eight Sprague-Dawley male rats, weighing 200 g were administered intraperitoneal via with 55 mg/kg from *streptozotocin* diluted in citrate buffer were housed in a temperature- and humidity-controlled room maintained on a 12-hour light/dark cycle (lights on: 07:00–19:00 hours) and had free access to food and water. Retinas were evaluated after 6 weeks from diabetic-induced.

The retinal mosaic was estimated for each subject (both eyes), at 270, 810, 1350 and 1890 μm of eccentricities from the optic nerve along the nasal, temporal, dorsal and ventral of both eyes. The photoreceptors arrangement was analyzed using Voronoi polygon and Delaunay triangulation analysis; estimations were done by using a sampling window S of $90 \times 90 \mu\text{m}$ image sections, **Figure 13**.

Through the Voronoi partition, some contours of the tessellations should be modified if other points outside the analysis window S ($90 \times 90 \mu\text{m}$) were acquired.

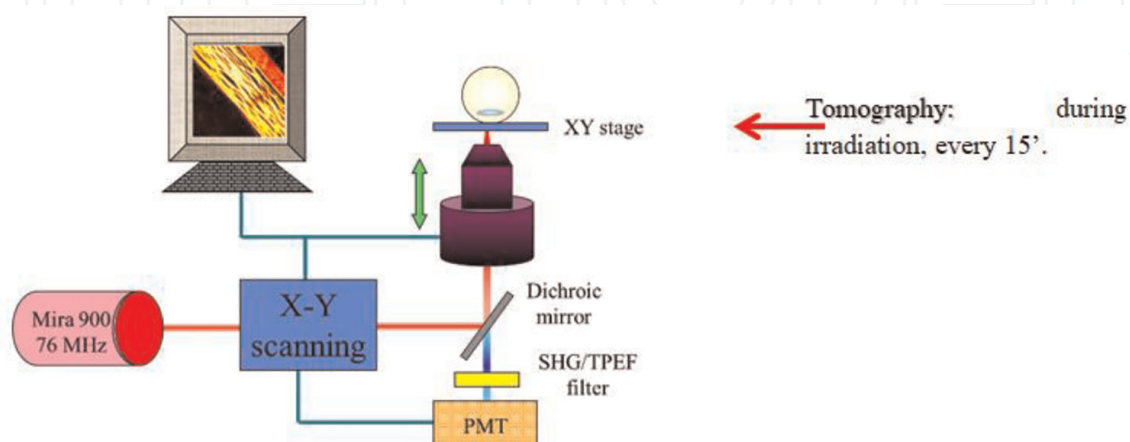


Figure 12.
 Setup for scanning with a multiphoton microscope.

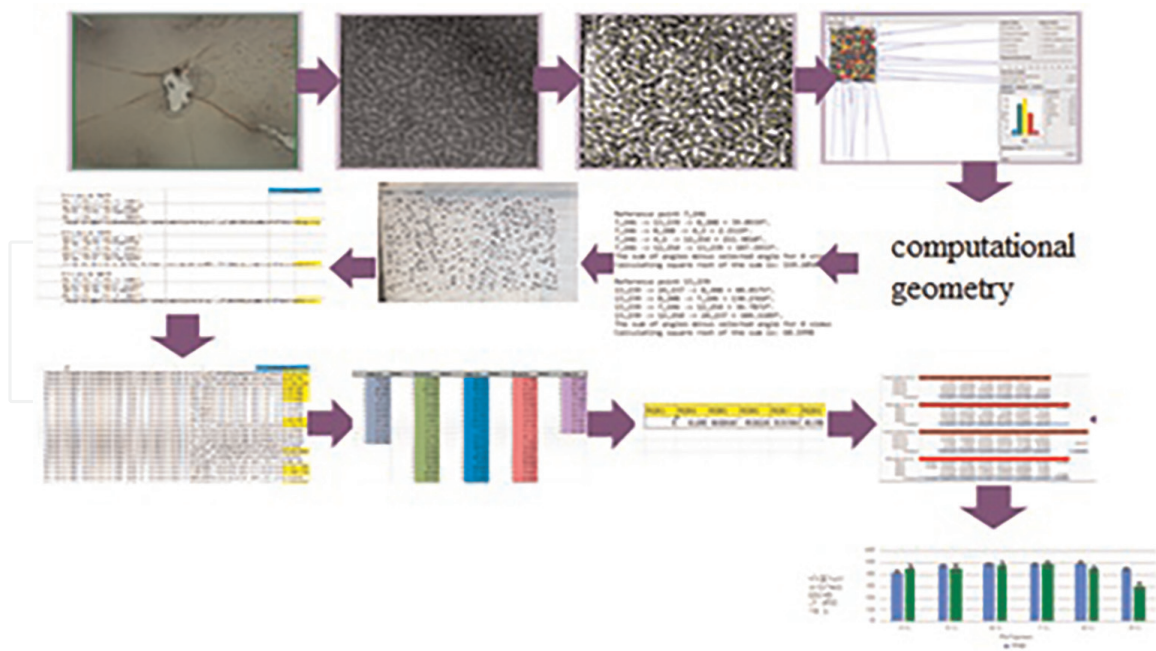


Figure 13. Data processing diagram in retinal tissues for healthy photoreceptors and with DR, starting from raw data and applying image processing and segmentation, feature extraction and classification, and finally polygonality measurements.

These points are associated to the outline regions which are closer to the analysis window than to the considered point. The points which belong to such contour regions are considered to be at the border. All the marginal points are not noted in the subsequent calculations, because they cause statistical noise.

4. Retinal tissues analysis

We use some metric/algorithms of Section 2.1 to analyze and model the polygonality in retinal tissues, especially with DR.

4.1 Mean-square deviation of angles

Using the metric of mean-square deviation of angles ε (Eq. (3)), to know the angular distributions of photoreceptors in the rodent retina in order to identify healthy tissues (C) from tissues with pathology (R). The results are shown in **Figure 14**.

Results obtained during this analysis reported that at an eccentricity of 270 μm , there is a greater angular variation than 6 degrees in 4-sided polygons in tissues with pathology (R) with respect to its counterpart of healthy tissues (C). At an eccentricity of 810 μm a greater angular variation is observed in polygons of 10 and 9 sides, in addition to polygons of 6 and 7 degrees, respectively, in tissues with pathology (R). At an eccentricity of 1350 μm , an angular variation is presented up to 12 degrees in polygons of nine sides in tissues with pathology (R). At an eccentricity of 1890 μm , again the 9-sided polygons present an angular variation of 9 degrees in tissues with pathology (R). Likewise, we identify that as the eccentricity increases; the training of a greater number of sides of polygons is increasing in tissues with pathology which does not present healthy tissues (not presented here).

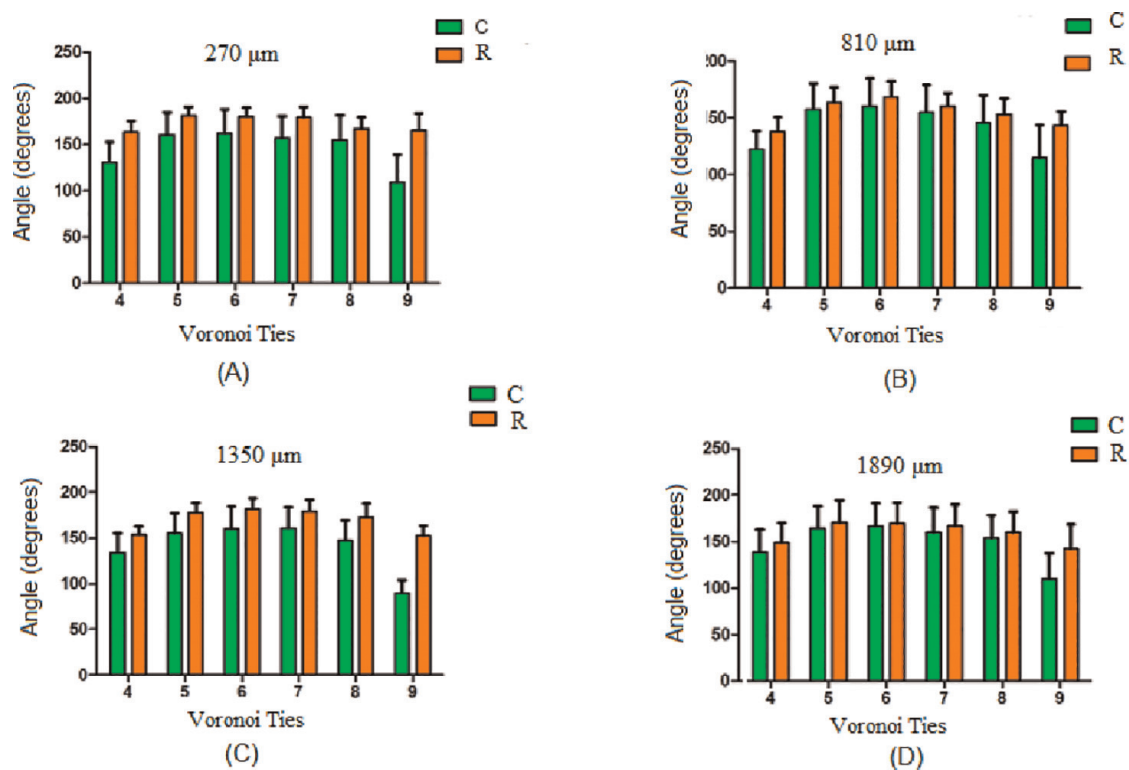


Figure 14.

Distribution of angular variation as eccentricity in retinal tissues, both healthy tissues (C) and diabetic retinopathy tissues (R): (A) 270 μm , (B) 810 μm , (C) 1350 μm , (D) 1890 μm .

Voronoi ties	P-value*		
	270 μm	1350 μm	1890 μm
5	0.006	0.002	0.022
6	0.025	0.0066	0.0204
7	0.001	0.018	0.0078

*Two-tailed.

Table 2.

P-value to 5, 6, and 7 Voronoi ties.

It is observed that if the angular variation is minor to 6.15 degrees, the value P is minor to 0.05. It is identified, then that to 810 and 1890 μm the angles of the polygons are minor to 30 degrees. For photography retinal, it is observed that to major eccentricity, the spacing of the photoreceptors is major, **Table 2**.

4.2 Detection of modal spacing

Using the metrics/algorithm of radius in a circumscribed circle for estimating photoreceptor spacing based on the circumradius of Delaunay triangle, as a metric that allows knowing how is the density/separation of photoreceptors in retinal healthy tissues and with diabetic retinopathy. This metric is an alternative form at the Yellott's ring [18]. The circumradius provides an estimation of the modal spacing in the retinal image of the photoreceptors. The distributions of density grouped by circumradius interval are: (a) 1.12–2.24 μm , (b) 2.244–3.36 μm , (c) 3.364–4.48 μm , (d)

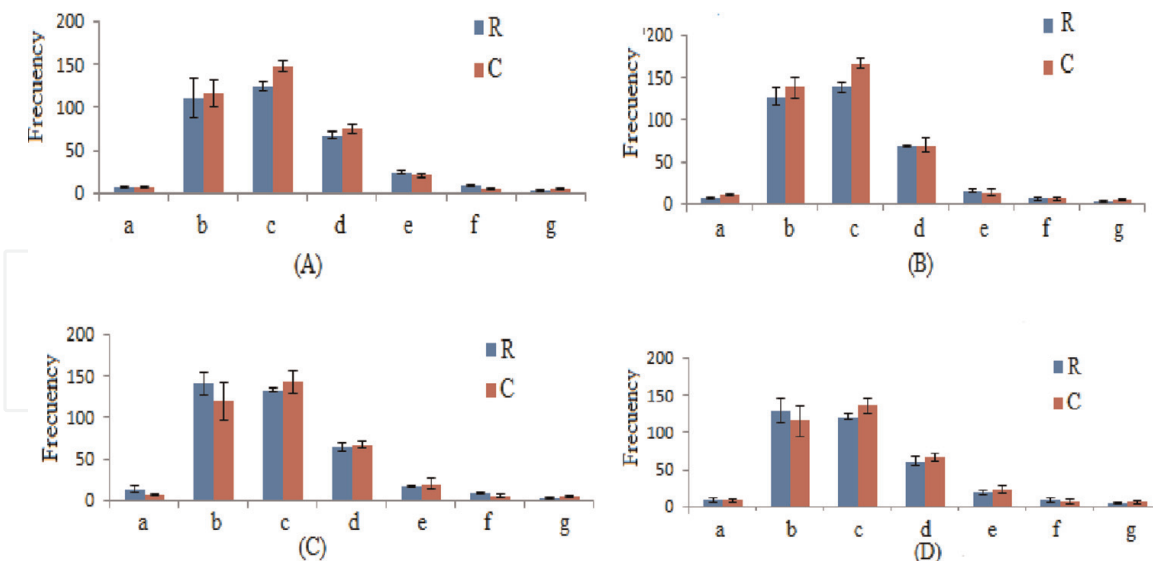


Figure 15. Distribution of spacing based on the circumradius grouped by eccentricity in retinal tissues: (A) 270 μm, (B) 810 μm, (C) 1350 μm, (D) 1890 μm.

4.485–5.601 μm, (e) 5.605–6.721 μm, (f) 6.725–7.842 μm, (g) 7.846–9.62 μm. The results are shown in **Figure 15**.

To distribute the density by spacing of photoreceptors, we have proposed a standard criterion for arbitrary intervals of circumradius: 1.12–2.24 μm, 2.244–3.36 μm, 3.364–4.48 μm, 4.485–5.601 μm, 5.605–6.721 μm, 6.725–7.842 μm, and 7.846–9.62 μm. By using these intervals with the metrics/algorithms of circumscribed circle to obtain each circumradius, our results allow us to observe that the two dominant distributions of grouped density of photoreceptors are at intervals between 3.364–4.48 μm and 2.244–3.36 μm.

With these results, it has been observed that the percentage of circumradius in the range of 2.244–3.36 μm increases in tissues with DR as eccentricity increases. These results show a density of separating healthy photoreceptors to 810 μm of eccentricity with circumradius in the range of 3.364–4.48 μm (42.51%) and in the range of 2.244–3.36 μm (37.68%), **Table 3**.

It has been also identified that in cellular damaged tissues with DR the training of circumradius to greater eccentricity and also with a larger radius increases, with

Retinal tissue	Range 3.364–4.48 μm	Range 2.24–3.36 μm	Eccentricity (μm)
R	38.75%	30%	270
C	41.59%	33.61%	270
R	37.42%	32.63%	810
C	42.51%	37.68%	810
R	34.35%	35.11%	1350
C	37.05%	36.04%	1350
R	33.24%	37.56%	1890
C	36.93%	38.69%	1890

Table 3. Percent density by eccentricity intervals.

Tissue	270 μm	810 μm	1350 μm	1890 μm
C	59.35 %	57.73 %	57.3 %	55.85%
R	55.68 %	56.9%	51.88 %	51.84%

Table 4.
 Percentage of circumradius in the interval $[3.364-5.601] \mu\text{m}$.

respect to the control tissue, this is because they increase the spaces between photoreceptors that stop emitting fluorescence. It is also appreciated that the clustered density decreases in the photoreceptors of tissues with diabetic retinopathy, between the intervals of $2.244-3.36 \mu\text{m}$ and in $3.364-4.48 \mu\text{m}$, as eccentricity.

However, in the interval $[3.364-5.601] \mu\text{m}$, that represents 55.8% of circumradius, they have a higher percentage behavior in control tissues than in tissues with DR, **Table 4**. Therefore, this shows that frequency of circumradius decreases in tissues with DR.

4.3 Mean distances average

To measure distances between neighbors that form each Voronoi cell is employed the metric/algorithm of mean distances average (Eq. (1)), as a measure for expansion or contraction of the polygon of Voronoi. The results are shown in **Figure 16**. This is a modification to the metric Ulam tree in each polygon. A measurement of spacing (or contraction) between neighbors is explained in terms of a bi-dimensional space with reference to the populations on flat surfaces. This metric allows us to measure the space between neighboring cells, as a result of leakage in photoreceptors.

In **Figure 16**, it can be seen that for the 5, 6 and 7-sided polygons, they have a similar spacing. In the same way it is observed that for polygons of four, eight and nine sides have a particular behavior of distance separating, the distances between diabetic cells increases, in relation to the healthy cells, because the distances between the cells increase because of the diabetic retinopathy.

Figure 16 depicts the mean averaged distance (Eq. (1)), as a function of the number of sides of Voronoi polygons for both control and pathological retinas. Since it

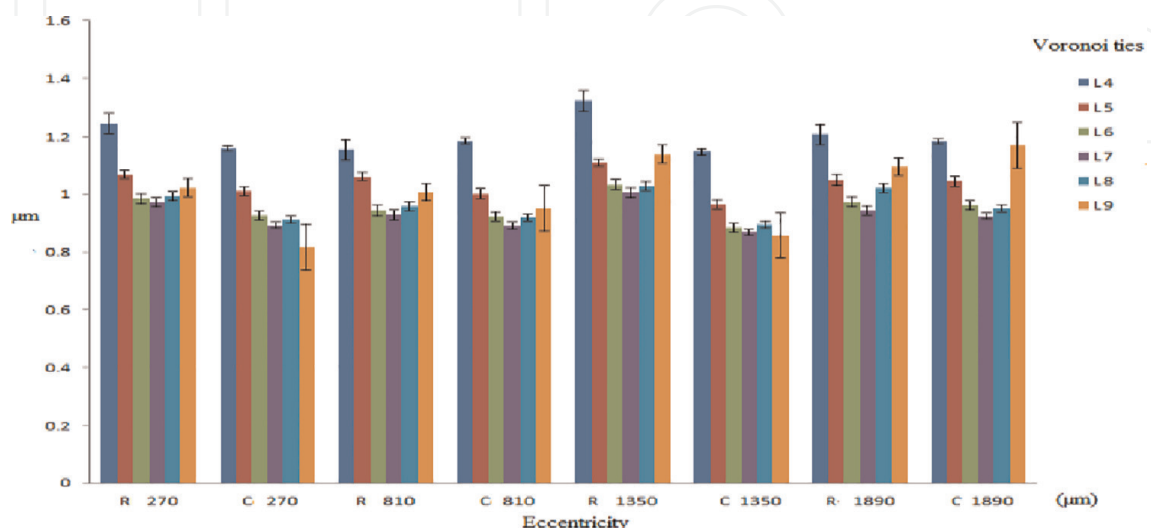


Figure 16.
 Distribution of cellular spacing in healthy tissue and with diabetic retinopathy according to the eccentricity measured from the optic nerve.

has been just showed that the polygon frequency distribution does not change with retinal eccentricity (**Figure 20**), the data have been also averaged across all locations for better comparisons. Differences between both groups of retinas were statistically significant (paired t -test, $P < 0.05$).

Using the Ulam tree modified for distances, it is possible to characterize the environment of each cell and in a more general way, to study cellular interactions. This metric/algorithm appears to be useful for analyzing the effects of the cell surrounding on a given cellular function and vice-versa.

A topic as suitable to determinate of the average type of the spatial occupation, following isoperimetric inequality [19], see Eq. (5),

$$L(X)^2 - 4\mu A(X)^2 \geq 0 \quad (5)$$

Where $A(X)$ is the area and $L(X)^2$ is the perimeter for a convex set.

4.4 Angular polygonality

With this metric/algorithm $\sum_{i=1}^{N_k} \frac{|\chi_i - \beta|}{n}$ is quantified that the Voronoi polygons of five, six, seven, and eight sides in healthy tissues and with diabetic retinopathy maintain a maximum range of angular values between 110 and 130 degrees measured from an arbitrary horizontal axis, defining an angular cluster of radio 10 degrees. It is shown that the Voronoi polygons of five, six, seven, and eight sides are sensitives.

However, the polygons of Voronoi in healthy tissues and with diabetic retinopathy of 3, 4, 9, 10, 11 and 12 sides are very irregular angularly, and the range of angular variation is from 60 to 180 degrees, defining an angular cluster radius of 60 degrees, **Figure 17**.

Other topics as suitable to capture regularity in convex Voronoi polygons is to measure how well they fit in a regular polygon or a regular polygon fits in them. This proposal has the characteristics to providing a way of fitting with convex polygons in

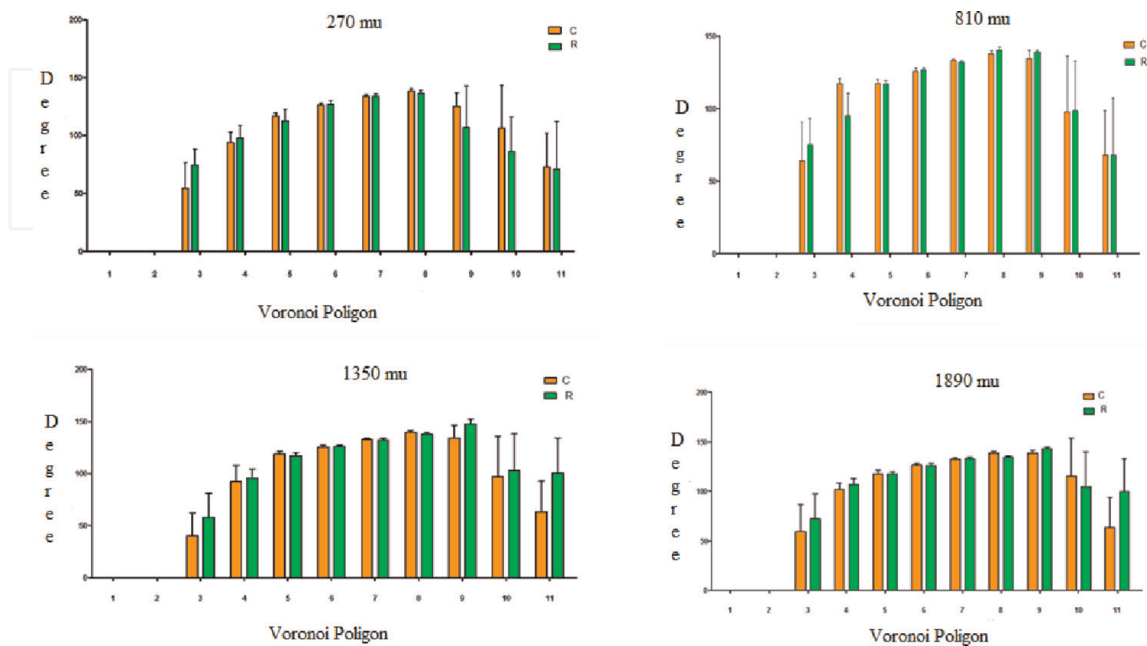


Figure 17. Distribution of the angular polygonality relative to the side number in the Voronoi polygon.

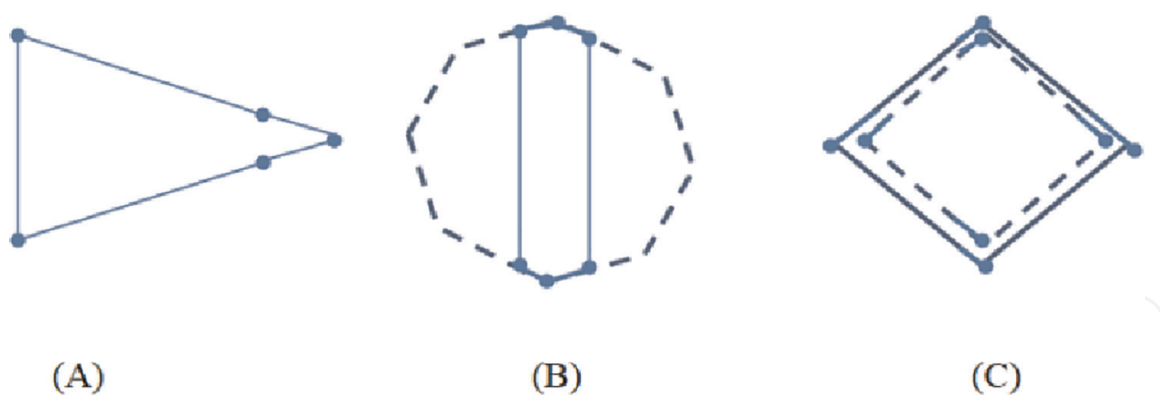


Figure 18.

In (A), a pentagon that almost looks like an equilateral triangle, (B) hexagon that almost looks like an octagon, (C) square that almost looks like a rhombus shape.

which they are very similar to regular polygons with a different number of edges [20], see **Figure 18**.

The procedure consists in transforming the given irregular polygon into a regular one, while measuring the amount of deformation required in such a process. The measurement of the angle variation gives a first parameter to consider in the final measurement of the regularity of Voronoi polygon. Using the Ulam tree modified to distances and the Ulam tree modified to angles gives a measure of the amount of deformation produced. Combining both procedures will be obtaining a measure of the regularity of the Voronoi tessellations on retinal tissues.

4.5 Frequency of Voronoi polygon

In order to quantify the distribution of polygons according to the eccentricity, frequency graphs were generated. In these it is observed that five and six sides polygons predominate, in healthy retinal tissues (C) and with diabetic retinopathy (R). In healthy tissues, with eccentricities of 270 and 810 μm , the frequency of polygons of five and six sides is greater, with respect to pathological tissues. However, with eccentricities of 1350 and 1890 μm , predominate 5-sided polygons, in tissues with diabetic retinopathy, **Figure 19**.

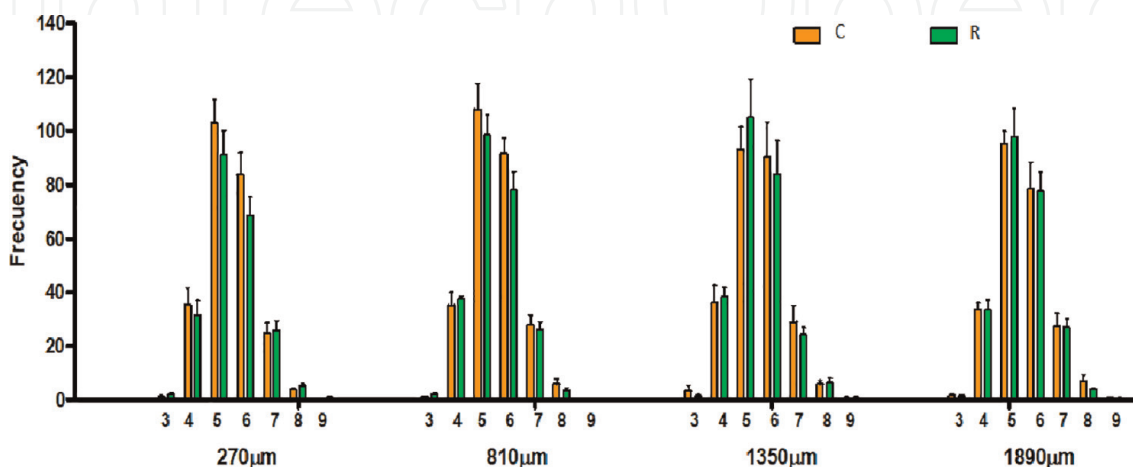


Figure 19.

Distribution of frequencies in Voronoi polygons by eccentricity in healthy retinal tissues (C) and with diabetic retinopathy (R).

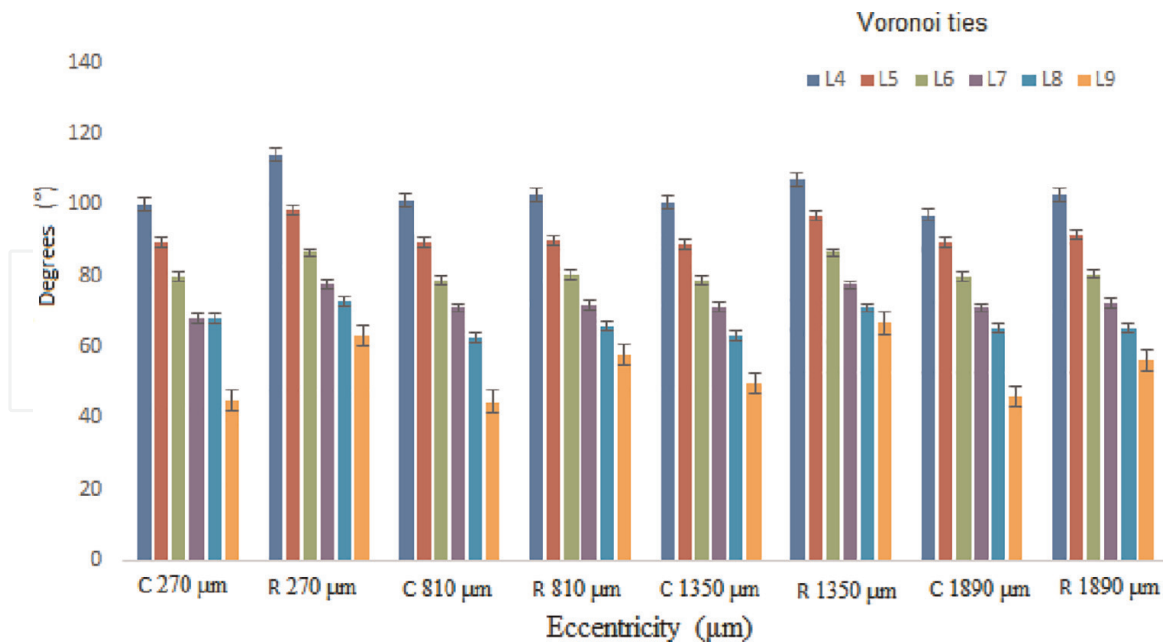


Figure 20. Distribution of maximum angles χ_i relative to the side number (4,5,6, ...) in the Voronoi polygon.

We found that the spatial sampling of the images with S window, even using resizing of the recorded images of $90 \times 90 \mu\text{m}$, has a significant impact on the performance of the metric/algorithms, but also that an excessive upsizing does not substantially improve the measurements. We observed that the percentage of Voronoi polygon is the parameter in which is most affected by errors in photoreceptors detection, and for this reason the combined measurements of more parameters could be a better choice in order to characterize different retinal regions and the different subjects' retinas.

4.6 Minimum and maximum angles

Control (C) and diabetic retinopathy (R) tissues were characterized based on measuring the maximum angles χ_i and minimum angles χ_i of the Delaunay triangles in Voronoi polygons (**Figure 5**). Greater sensitivity is identified when quantifying maximum angles than minimum angles; see **Figure 20** and **Table 5**.

5. Discussion

Soliman et al. [21], using AO fundus camera to acquired images of parafoveal cones, from patients with type II diabetes mellitus with or without retinopathy, captured the cone mosaic at 0 and 2 degrees eccentricities along the horizontal and vertical meridians. The density of the parafoveal cones was calculated within $100 \times 100\text{-}\mu\text{m}$ squares located at $500\text{-}\mu\text{m}$ from the foveal center along the orthogonal meridians. They found that the cone density was significantly lower in the moderate non-proliferative diabetic retinopathy (NPDR) and severe PDR/proliferative DR groups compared to the Control, No DR, and mild NPDR groups. Also, they found that the mean percentage of cones with hexagonal Voronoi tiles in the Control and No DR groups was 44.8% and 45.6%, respectively. In the DR groups, the percentage of cones with hexagonal Voronoi tiles ranged between 43.4% and 40.0%. They therefore

Voronoi ties	Control	Diabetic retinopathy	(±) Angular difference	P-value*
Maximum angles χ_i, 270 μm				
5	89.46	98.40	8.94	0.0208
6	79.75	86.66	6.91	0.0258
7	68.05	77.77	9.72	0.006
Maximum angles χ_i, 810 μm				
5	89.47	90.06	0.59	0.092
6	78.70	80.46	1.76	0.0596
7	71.09	71.90	0.81	0.0787
Maximum angles χ_i, 1350 μm				
5	88.79	97.11	8.32	0.0204
6	78.78	86.64	7.86	0.0198
7	71.30	77.45	6.15	0.0478
Maximum angles χ_i, 1890 μm				
5	89.63	91.51	1.88	0.06312
6	79.79	80.56	0.77	0.08258
7	71.13	72.25	1.12	0.07114

*Two-tailed.

Table 5.
Value-P for maximum angles in 5, 6 and 7 Voronoi ties.

conclude that decreased cone density may be linked to the prior use of anti-VEGF therapy in these patients. Since VEGF is known to have a neuroprotective effect on photoreceptors, anti-VEGF agents may potentially have a deleterious effect on photoreceptors. Other progress against the wet form of the disease has come through the use of drugs that target vascular endothelial growth factor, or VEGF, a substance in the body that promotes the growth of new blood vessels. It has also been found that, cone photoreceptor counts in the control group reported in this study fall within the range reported in previous studies, high inter subject variability of cone density may also play a significant role [22].

Likewise, Li and Roorda showed that the percentage of hexagonal Voronoi tended to decrease between 0.25 and 5 degrees from the fovea; a study on a post-mortem human retina showed that the cones were more hexagonally arranged near the edge of the fovea (between 0.20 and 0.25 degrees eccentricity) than in the foveal center [7, 23, 24]. According to the current study and previous work from others [25, 26] a model of the parafoveal mosaic by a lattice with continuous hexagonal regularity cannot be considered completely adequate to describe the cone mosaic arrangement in a healthy eye. In addition, in an AO retinal image of the photoreceptor mosaic, deviations from hexagonal order can be attributed to some phenomena, such as point defects and linear cracks. ‘Point defects’ of the cone lattice occur within otherwise intact mosaic areas and may be represented by smaller cones (S cones), cones with no wave guiding properties or isolated rods (it is plausible that rods cannot be always distinguished by point defects). Other phenomena that can contribute to change the hexagonal order

are represented by local variance of the cone shape and the compression along the vertical meridian as a consequence of the expansion along the horizontal meridian of the photoreceptor mosaic [7, 24, 27–29].

Lombardo [30] identified several possible limitations based on the preferred packing arrangement of the cone mosaic: resolution of AO system, study size, and the presence of several sources of confounding orbias. Firstly, the resolution of the rtx1 camera is insufficient to assess the density of extremely tightly packed cones at the center of the fovea. Whether or not this loss of parafoveal cones reflects similar changes at the foveal center remains unclear. To date, the association of photoreceptor loss and vision loss in patients with DR remains obscure. Secondly, small sample size is another limitation of this prospective observational cohort study. This variability could be attributed to several factors, including the lack of a standardized approach to cone counting and differences in image processing software, AO systems, sampling window size, and foveal reference point location.

Methodology based on the optical coherence tomography (OCT) allows it to quantify retinal thickness in diabetic retinopathy. A total of 136 patients in different stages of diabetic retinopathy were examined with OCT [31]. In the controls, retinal thickness was $153 \pm 15 \mu\text{m}$ in the fovea, $249 \pm 19 \mu\text{m}$ in the temporal parafoveal region, and $268 \pm 20 \mu\text{m}$ in the nasal parafoveal region. In diabetic patients, retinal thickness was increased to $307 \pm 136 \mu\text{m}$ in the fovea, $337 \pm 88 \mu\text{m}$ in the temporal retina, and $353 \pm 95 \mu\text{m}$ in the nasal retina, respectively. The differences between diabetics and controls were highly significant ($P < 0.001$). There was an intermediate correlation between retinal thickness and visual acuity, particularly in patients without macular ischemia. Sensitivity of detecting clinically significant macular edema by measuring foveal retinal thickness was 89% and specificity was 96%. Apparent correlation between the increase and decreased visual acuity in the retina thickness, can be explained by the results of an increase in the thickness will be related to the increase in time axonal loss. In diabetic retinopathy, retinal spaces can take place between the inner and outer plexiform layer, outer limiting membrane or the outer plexiform layer. These results demonstrate the retinal tissue integrity, as a measure of the retention axon connection, and as an index of visual function. The strength of the correlation between the retention structure and visual function as expected decreases in the eccentricity increases from the center of the fovea.

There is disagreement in the literature concerning the effects of age on PR packing density. Curcio et al. [32] found a nonsignificant change in the number of cone photoreceptors with age. However, they reported that the range of peak density variation at older ages was narrower, overlapping the lower end of the cone density from younger subjects.

As mentioned above, there are mixed results of histology on age-related changes in PR packing. It is clear that nonhuman primates undergo changes in the central retina with age [33, 34]. Ordy et al. [35] studied the visual acuity and foveal PR density in the retina of aged rhesus monkeys, finding that the foveal photoreceptor density decreased significantly in the oldest age group of macaque monkeys compared with the middle age group. Other properties of the photoreceptors have been found to change with age, in addition to the cone packing density. Gartner and Henkind [36] reported loss of photoreceptor nuclei. Keunen et al. [37] and Kilbride et al. [38] found that the cone pigment density decreased as a function of age. Elsner et al. [39] showed that young healthy people typically have steep foveal peaks in photopigment density, but older people have shallower distributions.

Our approach emphasizes the local density of the PR rather than the total area. Thus, we found that a significant decrease in photoreceptor packing density occurred primarily, at distances less than 1890 μm from the center of the fovea.

Changes in the central fovea are also evident from the analysis of foveal shape by Gorrard and Delori [40], who found that the curvature of the foveola increases with increasing age. Elsner et al. [39], Bone et al. [41], and Chang et al. [42] found changes in the distribution of macular pigment with age, but Delori [43] did not. Since macular pigment is deposited preferentially in the photoreceptor axons and inner plexiform layers of the retina. Similarly a loss of PR could cause an increased curvature. An alternative possibility is that central cones spread outward, and the foveal curvature increases due to this spread, but again, the mechanism would be more complex and not easily tested by PR packing measurements alone.

However, despite the seeming transparency of DR pathogenesis and the progress in its treatment observed in recent years, a number of issues remain that warrant further study [44–46]. One of them is the temporal sequence of pathological changes in DR development [47, 48]. Studies in rodents have highlighted that biomarkers of inflammation, such as leukostasis, overexpression of adhesion molecules in retinal vascular endothelial cells and leukocytes, vascular permeability alteration, and aggravated production of nitric oxide, prostaglandins, cytokines, and other inflammatory mediators appears in the retina during 1–6 months of diabetes crisis [49].

Most developed therapies for DR, have primarily focused on the terminal stage of this disease, and as thus, failed to address the early potentially reversible stage of this disease. In addition, most of these therapies have been associated with severe sight threatening side effects [44]. With that, understanding of the temporal sequence and stages of pathological disturbances of DR development is of great prognostic and scientific value, as it might contribute to improvements to current methods or even the development of new methods of diagnosis and treatment of such a serious complication of diabetes.

6. Conclusions

The general aim of this chapter was to establish an analysis for a comparison of retinal tissues with retinopathy diabetic and healthy tissues, which is an important problem to mechanically understanding of the processes that lead to the experimental observations.

In retinal tissues, metrics as quantification of Voronoi polygons and Delaunay triangles, are not sensitive to register changes in cellular organization, because in the first geometry, the number of dominant polygons are both six and five sides in both cases, and in the second geometry are presented the same amount of triangles Delaunay, as it has been reported by many authors [2–7]. Similarly, Kaccie and Roorda [50] showed that Voronoi regions gradually increase in size at higher eccentricities.

In this chapter, we focused here on the photoreceptor degeneration in an animal model of retinal degenerative disease, retinopathy diabetic, in which we investigate how pathology affects mosaic organization. We analyzed 128 retinal tissues here, eventually we found abnormality in retinal tissues. This spacing rule is enough to simulate the geometry of mosaics, suggesting that interactions between the mosaic cells satisfy tessellation formations of healthy tissues and pathological damaged

tissues. Once generated, cells migrate to their layer, and a simple rule controlling the spacing between cells of the same type suffices to control mosaic formation [51, 52]. This ensures uniform coverage of the retina by each type of cell, regarding the mechanisms that control the genesis of the different retinal cells.

From the Voronoi analyses, the parameter of Eq. (1), was also obtained. This has been reported to be very sensitive to changes in photoreceptors spacing [11]. Independently of the number of sides of the Voronoi polygons, the PR spacing increased in the samples with DR, what represents an expansion in cellular spacing.

Based on the results obtained, the metric that are suggested to detect morphological changes in retinal tissues with DR is the metric of the mean averaged distance (Eq. (1), **Figure 17**) and the mean square deviation of the angles (Eq. (3), **Table 2**), in both cases P value < 0.05 .

In this study, among the tools presented that are highly reliable and ready to be tested with human retinas are the mean averaged distance (Eq. (1)) and the mean square deviation of the angles (Eq. (3)), which have a high sensitivity to detect changes in DR tissues, by using retinal images obtained with a fundus camera or AOSLO. We consider that the tools mentioned (Eqs. (1) and (2)) are reliable enough to perform clinical level tests.

A much more effective developmental design, consistent with the experimental observations so far available, is that cell genesis and cell positioning are determined separately, which requires a combination of experimental and theoretical tools. Although we learn from comparing real data to obtain patterns, a mathematical model is needed to investigate the contribution from many retinal processes. The understanding of the distribution of cone density and spacing as a function of retinal eccentricity in the same eye and between fellow eyes of the same subject could be of great clinical utility when monitoring a subject longitudinally over time or when comparing controls with presumptive pathologic cases.

Several studies of diabetic retinopathy have focused especially on the retinal vasculature, but recent studies suggest that the neural retina also is involved. Oxidative stress and local inflammatory changes have been shown to play important roles in the pathogenesis of this retinopathy, but the source of reactive oxygen species has been less clear. Du et al. [53] accumulating evidence suggests that photoreceptor cells play a previously unappreciated role in the development of early stages of diabetic retinopathy, but the mechanism by which this occurs is not clear. The oxidative stress in retinas of diabetic mice emanates from neural photoreceptor cells, and elimination of these cells in diabetes inhibits both the oxidative stress and inflammatory changes shown to cause the vascular lesions of diabetic retinopathy. These studies suggest a mechanism by which neural cells can initiate the vascular injury characteristic of diabetic retinopathy.

Finally, we show in this chapter provides new insight into the mechanisms loss of cells observed of mice retinas, and could be used to rescue inner retinal neurons from secondary degeneration, enlarging the time window in which receptor transplants or substitution may be for the benefit of subjects suffering retinal degenerative diseases.

Conflict of interest

The authors declare that the research was conducted in the absence of any commercial or financial relationships that could be construed as a potential conflict of interest.

IntechOpen

Author details


Nazario Bautista-Elivar^{1*} and Ricardo Cruz-Castillo²

1 Electrical and Electronic Engineering Department, National Technological of Mexico/Technological Institute of Pachuca, Mexico

2 Academic Area of Mathematics and Physics, Institute of Basic Sciences and Engineering, Autonomous University of Hidalgo State, Mexico

*Address all correspondence to: nazario.be@pachuca.tecnm.mx

IntechOpen

© 2022 The Author(s). Licensee IntechOpen. This chapter is distributed under the terms of the Creative Commons Attribution License (<http://creativecommons.org/licenses/by/3.0>), which permits unrestricted use, distribution, and reproduction in any medium, provided the original work is properly cited. 

References

- [1] da Fontoura Costa L, Rocha F, Lima SMA. Characterizing polygonality in biological structures. *Physical Review E*. 2006;**73**:011913-10-011913-11
- [2] Song H, Chui TYP, Zhong Z, Elsner AE, Burns SA. Variation of cone photoreceptor retinal eccentricity with packing density and age. *Investigative Ophthalmology & Visual Science*. 2011; **52**:7376-7384
- [3] Li KY, Tiruveedhula P, Roorda A. Intersubject foveal photoreceptor variability of cone density in relation to eye length. *Investigative Ophthalmology & Visual Science*. 2010;**51**:6858-6867
- [4] Lombardo M, Serrao S, Ducoli P, Lombardo G. Variations in the image optical quality of the eye and the sampling limit of resolution of the cone mosaic in axial length with young adults. *Journal of Cataract and Refractive Surgery*. 2012;**38**:1147-1155
- [5] Garrioch R, Langlo C, Dubis AM, Cooper RF, Dubra A, Carroll J. Repeatability on in vivo cone spacing and density measurements. *Optometry and Vision Science*. 2012;**89**: 632-643
- [6] Hirsch J, Miller WH. Does resolution limit cone positional disorder? *Journal of the Optical Society of America*. 1992;**4**: 1481-1492
- [7] Curcio CA, Sloan KR. Packing human cone photoreceptors of geometry with eccentricity variation and evidence of the local anisotropy. *Visual Neuroscience*. 1992;**9**:169-180
- [8] Godara P, Siebe C, Rha J, Michaelides M, Carroll J. Assessing the photoreceptor mosaic over drusen using adaptive optics and SD-OCT. *Ophthalmic Surgery, Lasers & Imaging*. 2010;**41**:S104-S108
- [9] Godara P, Wagner-Schuman M, Rha J, Connor TB Jr, Stepien KE, Carroll J. Imaging the photoreceptor mosaic with adaptive optics: Beyond counting cones. *Advances in Experimental Medicine and Biology*. 2012;**723**:451-458
- [10] Okabe BA, B. and Sugihara, K. *Spatial Tessellations: Concepts and Applications of Voronoi diagrams*. New York: Wiley; 1992
- [11] Sudbø J, Marcelponil Reith R. New algorithms based on the Voronoi diagram applied in a pilot study on normal mucosa and carcinomas. *Analytical Cellular Pathology*. 2000;**21**: 71-86
- [12] Chiu SN. Spatial point pattern analysis by using Voronoi diagrams and Delanuy tessellations, a comparative study. *The Biochemical Journal*. 2003;**45**: 367-376
- [13] Headington K, Choi SS, Nickla D, Doble N. Single cell imaging of the chick retina with adaptive optics. *Current Eye Research*. 2011;**36**(10):947-957
- [14] Kisilak ML, Bunghardt K, Hunter JJ, Irving EL, Campbell MC. Longitudinal in vivo imaging of cones in the alert chicken. *Optometry and Vision Science*. 2012;**89**(5):644-651
- [15] Pinelis I. A characterization of the convexity of polygons in terms of cyclic center angles. *Journal of Geometry*. 2007;**87**(1):106-119
- [16] Rossi C, Strettoi E, Galli-Resta L. The spatial order of horizontal cells is not

affected by massive alterations in the organization of other retinal cells. The Journal of Neuroscience. 2003;23(30): 9924-9928

[17] Khiripe N, Khantuwan W, Jungck JR. Ka-me: A Voronoi image analyzer. Bioinformatics. 2012;28(13):1802-1804

[18] Cooper RF, Langlo CS, Dubra A, Carroll J. Automatic detection of modal spacing (Yellott's ring) in adaptive optics scanning light ophthalmoscope image. Ophthalmic & Physiological Optics. 2013;33(4):540-549

[19] Marcelpoil., R. and Usson, Y. Methods for the study of cellular sociology: Voronoi diagrams and parametrization of spatial relationships. Journal of Theoretical Biology. 1992;154: 359-369

[20] Chalmeta R, Hurtado F, Sacristan V, Saumell M. Measuring regularity of convex polygons. Computer-Aided Desing. 2013;45:93-104

[21] Soliman MK, Sadiq MA, Agarwal A, Sarwar S, Hassan M, Hanout M, et al. High-resolution imaging of parafoveal cones in different stages of diabetic retinopathy using adaptive optics fundus camera. PLoS One. 2016;11:1-13

[22] Curcio CA, Sloan KR, Kalina RE, Hendrickson AE. Human photoreceptor topography. Journal of Comparative Neurology. 1990;292(4):497-523

[23] Li KY, Roorda A. Automated identification of cone photoreceptors in adaptive optics retinal images. Journal of the Optical Society of America. A. 2007; 24:1358-1363

[24] Wojtas DH, Wu B, Ahnelt PK, Bones PJ, Millane RP. Automated analysis of differential interference contrast microscopy images of the foveal

cone mosaic. Journal of the Optical Society of America. A. 2008;25: 1181-1189

[25] da Fontoura CL, Oliveira Bonci DM, Saito CA, de Farias Rocha FA, de Lima Silveira LC, Ventura DF. Voronoi analysis uncovers relationship between mosaics of normally placed and displaced amacrine cells in the thraira retina. Neuroinformatics. 2005;5:59-77

[26] Hendrickson AE, Youdelis C. The morphological development of the human fovea. Ophthalmology. 1984;91: 603-612

[27] Chui TYP, Song H, Burns S. Adaptive-optics imaging of human cone photoreceptor distribution. Journal of the Optical Society of America. A. 2008; 25:3021-3029

[28] Williams DR. Topography of the foveal cone mosaic in the living human eye. Vision Research. 1988;28:433-454

[29] Pum D, Ahnelt PK, Grasl M. Iso-orientation areas in the foveal cone mosaic. Visual Neuroscience. 1990;5: 511-523

[30] Lombardo M, Serrao S, Ducoli P, Lombardo G. Eccentricity dependent changes of density, spacing and packing arrangement of parafoveal cones. Ophthalmic & Physiological Optics. 2013;33:516-526

[31] Goebel W, Kretzchmar-Gross T. Retinal thickness in diabetic retinopathy: A study using optical coherence tomography (OCT). Retina. 2002;22: 759-767

[32] Curcio CA, Millican CL, Allen KA, Kalina RE. Aging of the human photoreceptor mosaic: Evidence for selective vulnerability of rods in central

retina. *Investigative Ophthalmology & Visual Science*. 1993;**34**:3278-3296

[33] Francis PJ, Appukuttan B, Simmons E. Rhesus monkeys and humans share common susceptibility genes for age-related macular disease. *Human Molecular Genetics*. 2008;**17**:2673-2680

[34] Ulshafer RJ, Engel HM, Dawson WW, Allen CB, Kessler MJ. Macular degeneration in a community of rhesus monkeys: Ultrastructural observations. *Retina*. 1987;**7**:198-203

[35] Ordy JM, Brizzee KR, Hansche J. Visual-acuity and foveal cone density in the retina of the aged rhesus-monkey. *Neurobiology of Aging*. 1980;**1**:133-140

[36] Gartner S, Henkind P. Aging and degeneration of the human macula. 1. Outer nuclear layer and photoreceptors. *The British Journal of Ophthalmology*. 1981;**65**:23-28

[37] Keunen JEE, Norren DV, Meel GJV. Density of foveal cone pigments at older age. *Investigative Ophthalmology & Visual Science*. 1987;**28**:985-991

[38] Kilbride PE, Hutman LP, Fishman M, Read JS. Foveal cone pigment density difference in the aging human eye. *Vision Research*. 1986;**26**:321-325

[39] Elsner AE, Burns SA, Beausencourt E, Weiter JJ. Foveal cone photopigment distribution: Small alterations associated with macular pigment distribution. *Investigative Ophthalmology & Visual Science*. 1998;**39**:2394-2404

[40] Gorrand JM, Delori FC. Reflectance and curvature of the inner limiting membrane at the foveola. *Journal of the*

Optical Society of America. A. 1999;**16**:1229-1237

[41] Bone R, Landrum J, Fernandez L, Tarsis S. Analysis of the macular pigment by HPLC: Retinal distribution and age study. *Investigative Ophthalmology & Visual Science*. 1988;**29**:843-849

[42] Chang Y, Lee FL, Chen SJ, Chen SF. Optical measurement of human retinal macular pigment and its spatial distribution with age. *Medical Physics*. 2002;**29**:2621-2628

[43] Delori FC. Autofluorescence method to measure macular pigment optical densities fluorometry and autofluorescence imaging. *Archives of Biochemistry and Biophysics*. 2004;**430**:156-162

[44] Stitt AW, Lois N, Medina RJ, Adamson P, Curtis TM. Advances in our understanding of diabetic retinopathy. *Clinical Science (London, England)*. 2013;**125**:1-17

[45] El Rami H, Barham R, Sun JK, Silva PS. Evidence-based treatment of diabetic retinopathy. *Seminars in Ophthalmology*. 2017;**32**:67-74

[46] Rajalakshmi R, Prathiba V, Mohan V. Does tight control of systemic factors help in the management of diabetic retinopathy? *Indian Journal of Ophthalmology*. 2016;**64**:62-68

[47] Schorr SG, Hammes HP, Müller UA, Abholz HH, Landgraf R, Bertram B. The prevention and treatment of retinal complications in diabetes. *Deutsches Ärzteblatt International*. 2016;**113**:816-823

[48] Lechner J, O'Leary OE, Stitt AW. The pathology associated with diabetic retinopathy. *Vision Research*. 2017;**139**:7-14

[49] Chen M, Stitt A. Animal models of diabetic retinopathy. In: Chan CC, editor. *Animal Models of Ophthalmic Diseases*. Cham: Springer International Publishing; 2016. pp. 67-83

[50] Li KY, Roorda A. Automated identification of cone photoreceptors in adaptive retinal images. *Journal of the Optical Society of America. A*. 2007;**24**:5

[51] Galli-Resta L, Resta G, Tan S-S, Reese B. Mosaics of Islet-1 expressing amacrine cells assembled by short range cellular interactions. *The Journal of Neuroscience*. 1997;**17**:7831-7838

[52] Galli-Resta L. Assembling the vertebrate retina: Global patterning from short-range cellular interactions. *Neurology Report*. 2001;**12**:A103-A106

[53] Yunpeng D, Veenstra A, Palczewski K, Kerna TS. Photoreceptor cells are major contributors to diabetes-induced oxidative stress and local inflammation in the retina. *Proceedings of the National Academy of Sciences of the United States of America*. 2013;**41**: 16586-16591